# Nonequilibrium dynamical mean-field calculations based on the noncrossing approximation and its generalizations

Martin Eckstein and Philipp Werner
*Theoretical Physics, ETH Zurich, 8093 Zurich, Switzerland*
(Received 14 May 2010; published 17 September 2010)

We solve the impurity problem which arises within nonequilibrium dynamical mean-field theory for the Hubbard model by means of a self-consistent perturbation expansion around the atomic limit. While the lowest order, known as the noncrossing approximation (NCA), is reliable only when the interaction $U$ is much larger than the bandwidth, low-order corrections to the NCA turn out to be sufficient to reproduce numerically exact Monte Carlo results in a wide parameter range that covers the insulating phase and the metal-insulator crossover regime at not too low temperatures. As an application of the perturbative strong-coupling impurity solver we investigate the response of the double occupancy in the Mott insulating phase of the Hubbard model to a dynamical change in the interaction or the hopping, a technique which has been used as a probe of the Mott insulating state in ultracold fermionic gases.

DOI: 10.1103/PhysRevB.82.115115 PACS number(s): 71.10.Fd, 05.10.Ln

## I. INTRODUCTION

Experiments with ultracold atoms in optical lattices,[1] as well as pump-probe spectroscopy with femtosecond time-resolution[2–4] and transport measurements on quantum dots[5] enable a systematic investigation of strongly interacting quantum many-particle systems under nonequilibrium conditions. In a pump-probe experiment, a material is excited with a strong laser pulse, and its subsequent evolution is probed by a second pulse that reaches the sample at a controlled time delay. The breakdown of the Mott insulating phase within a few times of the inverse hopping has been observed in this way.[3,4] Ultracold gases in optical lattices, on the other hand, can be prepared in an equilibrium state and suddenly quenched out of equilibrium by modifying a Hamiltonian parameter.[6] These experiments can address fundamental questions such as the thermalization in isolated quantum systems.[7]

The ongoing experimental progress has stimulated intensive research on the theoretical side. While many theoretical approaches that are designed for the investigation of correlated systems in thermal equilibrium must be modified considerably before they can be used to compute the real-time evolution, dynamical mean-field theory (DMFT) (Ref. 8) is an approximate scheme which can be used both for equilibrium and nonequilibrium situations.[9] The method relies on a mapping of lattice models to a single impurity model, which is exact in the limit of infinite dimensions,[10] and provides a good basis for the realistic simulation of many correlated materials.[11] Nonequilibrium DMFT has so far been used, e.g., to study transport beyond linear response in the Falicov-Kimball model,[12–15] as well as interaction quenches and interaction ramps in the Falicov-Kimball model[16,17] and in the Hubbard model.[18,19] In the last part of this paper we will use DMFT to study the response of the Mott insulating phase to a periodic modulation of the hopping or the interaction,[20] similar to what can now be done in experiments with cold atomic gases.[21,22]

Currently, the biggest challenge within the context of nonequilibrium DMFT is the development of impurity solvers which allow to compute the long-time dynamics after a perturbation. An exact solution, via a closed set of equations of motion, is known only for the Falicov-Kimball model.[12,23] For the Hubbard model, continuous-time quantum Monte Carlo (CTQMC) can, in principle, be used to obtain an unbiased solution.[18,19] Both the weak-coupling expansion[24] and the strong-coupling expansion[25] of the relevant Anderson impurity model have been translated from their respective imaginary-time variants (Refs. 26 and 27 for weak coupling and Ref. 28 for strong coupling) to the Keldysh formalism, in order to study the real-time evolution. However, in these real-time Monte Carlo calculations, the accessible times are limited by the notorious dynamical sign problem. A big advantage of the weak-coupling expansion over the strong-coupling expansion is that the diagrammatic series simplifies in the case of particle-hole symmetry.[29] On the other hand, the sign problem in a weak-coupling calculation increases with the interaction strength. It is thus essentially impossible to use CTQMC to study complex excitation processes within the Mott insulating phase, e.g., the excitation with a short laser pulse and the subsequent relaxation.

In order to avoid the sign problem and access the regime of strong interactions and relatively long times, we explore the direct summation of the self-consistent diagrammatic hybridization expansion up to fixed order, as opposed to CTQMC, which is in essence a stochastic summation of the full (nonself-consistent) series. This approach proves to be very accurate in a wide parameter regime and suitable for the calculation of the real-time dynamics.

Systematic approximations for the expansion around the atomic limit of the Anderson impurity model have been used for a long time.[30–36] The simplest conserving approximation, which has been termed noncrossing approximation (NCA), can correctly recover the Kondo temperature $T_K$ when charge fluctuations are suppressed completely by the Coulomb interaction $U$, although the Fermi-liquid behavior for $T \ll T_K$ is not correctly reproduced.[36,37] If $U$ is finite, however, the width of the Kondo resonance is severely underestimated and various resummation schemes of the expansion have been devised to cure this problem.[38,39] Already the simplest

 

correction to NCA within these schemes, the so called one-crossing approximation (OCA), can cure the deficiencies of NCA to a large extent. Motivated by the fact that NCA is already very good in the insulating parameter regime, Gull *et al.*[40] recently developed a bold-line hybridization expansion, i.e., an approach which is based on a Monte Carlo sampling of the corrections beyond NCA.

Starting with the work of Pruschke *et al.*,[41] both the NCA and the OCA have been used as an impurity solver for DMFT (for some recent references that involve the investigation of real materials, see Refs. 42–44). Furthermore, NCA and its corrections can readily be translated into the Keldysh formalism to study nonequilibrium situations, although the evaluation of higher order diagrams in real time involves quite some numerical effort. For example, the buildup of the Kondo resonance after a sudden shift of the impurity level in the Kondo model has been investigated with NCA.[45] The fairly accurate results in equilibrium calculations and the straightforward portability to the Keldysh contour make the self-consistent hybridization expansion an interesting candidate for the solution of the impurity problem within nonequilibrium DMFT.

The purpose of this paper is twofold. First, we give a detailed description of the self-consistent expansion on the Keldysh contour (Secs. II and III) and we benchmark the method by applying it to the interaction quench in the Hubbard model on the Bethe lattice (Sec. IV). We find similar trends for both equilibrium and nonequilibrium: While NCA is unreliable unless the interaction $U$ is much larger than the bandwidth, OCA provides an important correction, and the third order is in almost quantitative agreement with QMC results over a wide parameter range which includes the insulating phase and the crossover regime between metal and insulator. As an application of the perturbative impurity solver we then study the excitation of a Mott insulator by a time-dependent modulation of the hopping or the interaction strength (Sec. V). Because the interaction is rather large in this problem, a solution using weak-coupling CTQMC is currently not feasible.

## II. DEFINITION OF THE IMPURITY PROBLEM ON THE KELDYSH CONTOUR

To describe a nonequilibrium situation in which the system is prepared in a thermal equilibrium state at temperature $T=1/\beta$ for times $t<0$ and later acted on by some perturbation, we use the Keldysh formalism.[46,47] The imaginary-time contour of the Matsubara Green's functions for finite-temperature equilibrium states is thereby extended to the L-shaped contour $\mathcal{C}$ that runs from 0 to time $t_{\max}$ (i.e., the largest time of interest) along the real axis, back to 0, and finally to $-i\beta$ along the imaginary time axis (Fig. 1). The Keldysh formalism is based on the use of contour-ordered correlation functions $\langle T_{\mathcal{C}} A(t_1)B(t_2)\rangle$, where $T_{\mathcal{C}}$ exchanges the order of the two operators $A(t_1)$ and $B(t_2)$ in the product $A(t_1)B(t_2)$ if $t_2$ appears later on the contour than $t_1$, according to the order which is indicated by the arrows in Fig. 1. An additional minus sign appears if the exchange involves an odd number of Fermi operators. The use of contour-ordered

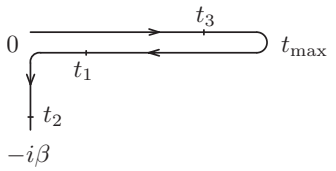


FIG. 1. The L-shaped contour $\mathcal{C}$ for the description of transient nonequilibrium states with initial state density matrix $\propto\exp[-\beta H(0)]$. The indicated time arguments are in cyclic order, $t_1<t_2<t_3$ (see text).

Green's functions allows the application of Wick's theorem if the action is quadratic.[46] Depending on the choice of the time arguments, a contour-ordered correlation function describes either real-time correlations, or it recovers the imaginary-time ordered correlation function of the initial equilibrium state.

In the following sections we consider an impurity model which is defined by the following action on the L-shaped contour $\mathcal{C}$:

$$\mathcal{S}_{\rm imp} = \mathcal{S}_{\rm loc} + \mathcal{S}_{\rm hyb}, \tag{1a}$$

$$\mathcal{S}_{\rm loc} = -i\int_{\mathcal{C}} dt H_{\rm loc}[d_p^\dagger(t), d_p(t), t], \tag{1b}$$

$$\mathcal{S}_{\rm hyb} = -i\int_{\mathcal{C}} dt_1 dt_2 \sum_{p_1,p_2} d_{p_1}^\dagger(t_1)\Lambda_{p_1,p_2}(t_1,t_2)d_{p_2}(t_2). \tag{1c}$$

In this action, $d_p$ and $d_p^\dagger$ denote annihilation and creation operators for an electron in the impurity level $p$ ($p$ labels spin and orbital degrees of freedom), and $H_{\rm loc}$ is the local Hamiltonian of the impurity site, which can be interacting and time-dependent in general. The hybridization function $\Lambda_{p_1,p_2}(t_1,t_2)$ gives the amplitude for the hopping of an electron from the $p_2$ orbital into the bath at time $t_2$, its propagation within the bath and the hopping back into the impurity orbital $p_1$ at time $t_1$. The action in Eq. (1) can be derived from an impurity Hamiltonian with time-dependent coupling between bath and impurity

$$H(t) = H_{\rm loc}(t) + \sum_\nu \epsilon_\nu c_\nu^\dagger c_\nu + \sum_{p,\nu}[V_{p,\nu}(t)d_p^\dagger c_\nu + \text{H.c.}] \tag{2}$$

by tracing out the bath degrees of freedom $c_\nu$. It also arises as the effective single-site problem in nonequilibrium DMFT (Ref. 12) without direct reference to a given Hamiltonian formulation.

The single-particle Green's function of the impurity model in Eq. (1) is given by

$$G_{p,p'}(t,t') = -i\langle d_p(t)d_{p'}^\dagger(t')\rangle_{\mathcal{S}_{\rm imp}}, \tag{3}$$

where the contour-ordered expectation value for the action $\mathcal{S}$ is defined as

$$\langle \cdots \rangle_{\mathcal{S}} = \frac{\mathrm{Tr}[T_{\mathcal{C}} \exp(\mathcal{S}) \cdots]}{\mathrm{Tr}[T_{\mathcal{C}} \exp(\mathcal{S})]}. \tag{4}$$

The nonequilibrium formalism presented below reduces to the Matsubara formalism for the initial equilibrium state when all calculations are restricted to the imaginary branch of the contour. For time-arguments $t=-i\tau$ and $t'=-i\tau'$ on the imaginary branch of $\mathcal{C}$, the Green's function $G(t,t')$ is directly related to the Matsubara Green's function $G^{\mathrm{M}}(\tau)$ of the initial thermal equilibrium state,

$$G(-i\tau,-i\tau') \equiv iG^{\mathrm{M}}(\tau-\tau'), \tag{5}$$

which is translationally invariant in time. An analogous equation is used to define the Matsubara component of all two-time contour-ordered correlation functions that are used in the following. The factor $i$ on the right-hand side of Eq. (5) is needed to recover the conventional definition of the Matsubara functions.

## III. SELF-CONSISTENT DIAGRAMMATIC HYBRIDIZATION EXPANSION OF THE ANDERSON IMPURITY MODEL

### A. Pseudoparticle representation

In this section we compute the Green's function in Eq. (3) by expanding the expectation value in Eq. (4) in terms of the hybridization function $\Lambda(t,t')$. The self-consistent hybridization expansion for the Anderson model in thermal equilibrium has been described previously in many places[30–36,38,39,44] and the generalization from the imaginary-time contour to the Keldysh contour is rather straightforward. Nevertheless we give a detailed derivation below, in order to discuss some important technical differences between the equilibrium and the nonequilibrium variants of the expansion.

Because the local part in Eq. (1b) of the action is generally not quadratic, standard diagrammatic perturbation theory does not apply to the expansion around the atomic limit ($\Lambda=0$). There exist several related strategies to bypass this difficulty. In the CTQMC variant of the hybridization expansion,[28] high-order time-ordered correlation functions of the impurity problem are explicitly evaluated in a suitable basis of the local problem. We will follow a different approach, which is based on the introduction of auxiliary particles.[33,34] This allows to use standard resummation tricks from diagrammatic perturbation theory, at the expense of having to do a projection from the extended pseudoparticle Hilbert space to the physical Hilbert space.

The local part $H_{\mathrm{loc}}(t)$ of the impurity Hamiltonian is written in a local basis $|m\rangle$, which we choose time-independent in the following:

$$H_{\mathrm{loc}}(t) = \sum_{mm'} |m\rangle h_{mm'}(t) \langle m'|. \tag{6}$$

For each state $m$ one flavor of pseudoparticles, with annihilation (creation) operator $a_m^{(\dagger)}$, is introduced, which is bosonic if the state $|m\rangle$ corresponds to an even number of particles on the impurity, and fermionic otherwise. (It is assumed that $H_{\mathrm{loc}}$ does not mix particle number states). Note that in many situations, $H_{\mathrm{loc}}(t)$ is diagonal in the basis $|m\rangle$ although the eigenenergies depend on time. In Sec. V below, e.g., $|m\rangle$ will be the occupation number basis and the density-density Coulomb interaction changes with time. However, in other important cases, such as the presence of time-dependent transverse magnetic fields, the eigenbasis of the local problem can indeed be time-dependent.

By means of the isomorphy $|m\rangle \leftrightarrow a_m^\dagger|\mathrm{vac}\rangle$, the physical Hilbert space of the impurity can be identified with the subspace of the pseudoparticle Fock space in which the total number of pseudoparticles

$$Q = \sum_m a_m^\dagger a_m \tag{7}$$

is exactly one. Hence the expectation value $\langle A(t)\rangle_{\mathcal{S}_{\mathrm{imp}}}$ of any impurity observable $A$ can be computed in the pseudoparticle space as

$$\langle A(t)\rangle_{\mathcal{S}_{\mathrm{imp}}} = \langle \tilde{A}(t)\rangle_{Q=1} \equiv \frac{\langle \delta_{Q,1}\tilde{A}(t)\rangle_{\tilde{\mathcal{S}}_{\mathrm{imp}}}}{\langle \delta_{Q,1}\rangle_{\tilde{\mathcal{S}}_{\mathrm{imp}}}} \tag{8}$$

provided that the pseudoparticle action $\tilde{\mathcal{S}}_{\mathrm{imp}}$ and the observable $\tilde{A}$ are constructed such that they coincide with $\mathcal{S}_{\mathrm{imp}}$ and $A$ in the $Q=1$ subspace ($\delta_{Q,1}$ is the projection onto $Q=1$). The requirement is satisfied by choosing

$$\tilde{d}_p^\dagger = \sum_{m,n} F_{mn}^p a_m^\dagger a_n, \tag{9a}$$

$$\tilde{d}_p = \sum_{m,n} (F_{nm}^p)^* a_m^\dagger a_n, \tag{9b}$$

$$F_{mn}^p = \langle m|d_p^\dagger|n\rangle \tag{9c}$$

for the electron annihilation and creation operators, and

$$\tilde{\mathcal{S}}_{\mathrm{loc}} = -i\sum_{mn} \int_{\mathcal{C}} dt h_{mm'}(t) a_m^\dagger(t) a_{m'}(t), \tag{10a}$$

$$\tilde{\mathcal{S}}_{\mathrm{hyb}} = -i \sum_{m,n,m',n'} \sum_{p,p'} \int_{\mathcal{C}} dt dt' a_m^\dagger(t) a_n(t) \times F_{mn}^p \Lambda_{p,p'}(t,t') (F_{n'm'}^{p'})^* a_{m'}^\dagger(t') a_{n'}(t') \tag{10b}$$

for the impurity action. The first line in Eq. (10) follows from Eqs. (1b) and (6), and the second line results from the insertion of Eqs. (9) into Eq. (1c).

Feynman diagrams for pseudoparticle propagators are most easily constructed in the grand-canonical ensemble with respect to the total pseudoparticle number $Q$. For this purpose it is convenient to switch into the interaction representation with respect to a chemical potential term $\lambda Q$. Because $Q$ is a conserved quantity, the value of $\lambda$ for $t>0$ has no influence on the expectation value of physical observables. We choose $\lambda$ to be present only at times $t<0$, (i.e., on the imaginary part of the contour, where $t=-i\tau$), such that

$$a_m(t) = a_m \exp(\lambda\ \mathrm{Im}\ t), \tag{11a}$$

$$a_m^\dagger(t) = a_m^\dagger \exp(-\lambda \,\mathrm{Im}\, t) \tag{11b}$$

and the grand canonical average can be denoted as

$$\langle \tilde{A}(t)\rangle_\lambda = \frac{\langle e^{-\beta\lambda Q}\tilde{A}(t)\rangle_{\tilde{S}_{\mathrm{imp}}}}{\langle e^{-\beta\lambda Q}\rangle_{\tilde{S}_{\mathrm{imp}}}}. \tag{12}$$

Grand-canonical pseudoparticle propagators on the contour $\mathcal{C}$ are defined as

$$\mathcal{G}^\lambda_{mm'}(t,t') = -i\langle T_{\mathcal{C}} a_m(t) a^\dagger_{m'}(t')\rangle_\lambda. \tag{13}$$

(In the following, propagators are considered to be matrices in their flavor indices $m,m'$ and the indices will be omitted whenever this is not ambiguous.)

The restricted trace in Eq. (8) can be recovered from grand-canonical expectation values by means of an expansion in powers of the fugacity $\zeta = e^{-\beta\lambda}$.[34] For observables which annihilate the $Q=0$ state [such as the impurity Green's function in Eq. (3)], an expansion of Eq. (12) in $\zeta$ yields

$$\frac{\langle \tilde{A}(t)\rangle_\lambda}{\langle Q\rangle_\lambda} = \langle \tilde{A}(t)\rangle_{Q=1} + \mathcal{O}(\zeta). \tag{14}$$

Furthermore, the leading terms of the Green's functions in Eq. (13) in the fugacity expansion can be obtained in the form [cf. Eq. (11)]

$$\mathcal{G}^\lambda(t,t') = k_\lambda(t,t')[\mathcal{G}(t,t') + \mathcal{O}(\zeta)], \tag{15}$$

where the *projected Green's function* $\mathcal{G}(t,t')$ is independent of $\lambda$ and the prefactor is given by

$$k_\lambda(t,t') = e^{\lambda(\mathrm{Im}\, t - \mathrm{Im}\, t')}[\Theta_{\mathcal{C}}(t,t') + \Theta_{\mathcal{C}}(t',t)\zeta]. \tag{16}$$

The step function $\Theta_{\mathcal{C}}(t,t')$ is 0 if $t$ is earlier on $\mathcal{C}$ than $t'$, and 1 otherwise. In order to obtain a perturbation expansion directly in terms of projected quantities, the limit $\lambda\to\infty$ must be taken analytically in all expressions below. As a consequence, projected Green's functions become the basic objects in the hybridization expansion.

In addition to the symmetries of the grand-canonical propagators,[47] projected propagators have a number of useful properties, which we list in the following paragraph. First, one can show from their definition that they satisfy an initial condition

$$\mathcal{G}_{mm'}(t^+,t) = -i\delta_{mm'}, \tag{17}$$

when $t^+$ is infinitesimally later on $\mathcal{C}$ than $t$. Furthermore, the factor $k_\lambda$ essentially restricts propagation of pseudoparticles to one direction along the contour. In particular, the leading order of the product of two Green's functions $A^\lambda$ and $B^\lambda$ is given by

$$A^\lambda(t,t_1)B^\lambda(t_1,t') \sim k_\lambda(t,t')A(t,t_1)B(t_1,t') \tag{18}$$

if the time arguments $t'$, $t_1$, and $t$ are in cyclic order with respect to the arrow in Fig. 1, and smaller by a factor $\zeta$ otherwise. [In the following, we will use the notation $t_1 \prec t_2 \prec \cdots \prec t_n$ to indicate that time arguments $t_1,\ldots,t_n$ are in cyclic order along $\mathcal{C}$, according to the arrow in Fig. 1.] Consequently, to leading order in $\zeta$ the contour convolution of the two functions is given by

$$\int_{\mathcal{C}} d\bar{t} A^\lambda(t,\bar{t})B^\lambda(\bar{t},t') = k_\lambda(t,t')\int_{\mathcal{C},t'\prec\bar{t}\prec t} d\bar{t} A(t,\bar{t})B(\bar{t},t'), \tag{19}$$

where the integration range on the right-hand side must be restricted such that $t' \prec \bar{t} \prec t$.

### B. Pseudoparticle Dyson equation

Grand-canonical pseudoparticle propagators obey the usual Dyson equation with the pseudoparticle self-energy $\Sigma^\lambda$

$$\mathcal{G}^\lambda = \mathcal{G}^\lambda_0 + \mathcal{G}^\lambda_0 * \Sigma^\lambda * \mathcal{G}^\lambda, \tag{20}$$

where $[a*b](t,t') = \int_{\mathcal{C}} d\bar{t} a(t,\bar{t})b(\bar{t},t')$ denotes the contour convolution and

$$\mathcal{G}^\lambda_{0,mm'}(t,t') = -i\langle a_m(t)a^\dagger_{m'}(t')\rangle_{\tilde{S}_{\mathrm{loc}},\lambda} \tag{21}$$

is the bare pseudoparticle propagator (i.e., at zero hybridization). The latter satisfies the equation of motion

$$[i\partial_t - \lambda(t) - h(t)]\mathcal{G}^\lambda_0(t,t') = \delta_{\mathcal{C}}(t,t'), \tag{22}$$

where $\lambda(t)=\lambda$ on the imaginary part of the contour and zero otherwise and $[h(t)]_{mm'} = h_{mm'}(t)$ is the local Hamiltonian as a matrix in the flavor indices [cf. Eq. (6)]. We use the notation of Ref. 19 for the derivative $\partial_t$ and the contour delta function $\delta_{\mathcal{C}}$, i.e., the latter is defined such that $\int_{\mathcal{C}} d\bar{t}\delta_{\mathcal{C}}(t,\bar{t})f(\bar{t}) = f(t)$ holds for any function $f(t)$ on $\mathcal{C}$, and $\partial_t\Theta_{\mathcal{C}}(t,t') = \delta_{\mathcal{C}}(t,t')$.

Although we will not need an explicit expression for the bare projected propagator $\mathcal{G}_0(t,t')$ in the following, it may be a useful illustration to compute it from the equation of motion in Eq. (22), and verify that it satisfies all the usual symmetries of the contour Green's functions[47] and the initial condition in Eq. (17). We will do this for the special case in which the local Hamiltonian is diagonal in the basis $|m\rangle$, $h_{mm'}(t) = E_m(t)\delta_{mm'}$: by integrating Eq. (22) with a periodic or antiperiodic boundary condition for Bose and Fermi particles, respectively, we obtain the grand-canonical propagator

$$\mathcal{G}^\lambda_0(t,t') = -ie^{\lambda(\mathrm{Im}\, t - \mathrm{Im}\, t')}\frac{\exp\left[-i\int_{t'}^{t} d\bar{t}E(\bar{t})\right]}{e^{\beta[\lambda+E(0)]} - \chi} \times [e^{\beta[\lambda+E(0)]}\Theta_{\mathcal{C}}(t,t') + \chi\Theta_{\mathcal{C}}(t',t)], \tag{23}$$

where $\chi=+1(-1)$ for Bose (Fermi) particles, and $E(0)$ is the value on the imaginary time axis. Taking the limit $\lambda\to\infty$ in this expressions yields $\mathcal{G}^\lambda_0(t,t') = k_\lambda(t,t')\mathcal{G}_0(t,t')$, with the projected propagator

$$\mathcal{G}_0(t,t') = -ie^{-i\int_{t'}^{t} d\bar{t}E(\bar{t})}[\Theta_{\mathcal{C}}(t,t') + \chi e^{-\beta E(0)}\Theta_{\mathcal{C}}(t',t)]. \tag{24}$$

Using Eq. (22), the Dyson equation can be written in differential form

$$[i\partial_t - \lambda(t) - h(t)]\mathcal{G}^{\lambda}(t,t') - [\Sigma^{\lambda} * \mathcal{G}^{\lambda}](t,t') = \delta_{\mathcal{C}}(t,t'). \tag{25}$$

The corresponding Dyson equation for the projected propagators is then derived by inserting Eqs. (15), (16), and (19) into Eq. (25), and taking the limit $\lambda \to \infty$

$$[i\partial_t - h(t)]\mathcal{G}(t,t') - \int_{\mathcal{C},t'<\bar{t}<t} d\bar{t}\Sigma(t,\bar{t})\mathcal{G}(\bar{t},t') = 0. \tag{26}$$

The delta function on the right-hand side has been omitted because this equation will be considered only for $t \neq t'$.

The numerical solution of Eq. (26) can be performed in the same way as the solution of Dyson-type equations for real-particle propagators, which is described in detail in Ref. 19. However, the structure of the integral in Eq. (26) implies an important simplification. In Eq. (26), the derivative $\partial_t \mathcal{G}(t,t')$ is determined entirely by the value of $\mathcal{G}(t_1,t')$ for $t' < t_1 < t$. For fixed $t'$, Eq. (26) is thus a Volterra integrodifferential equation,[48] whose numerical solution is similar to that of an ordinary differential equation with initial condition specified in Eq. (17). This is particularly interesting for the initial state, i.e., when all time arguments are on the imaginary branch of the contour. Substituting the definition in Eq. (5) into Eqs. (25) and (26) yields

$$(-\partial_\tau - \lambda - h)\mathcal{G}^{\lambda,\mathrm{M}}(\tau) - \int_0^\beta d\bar{\tau}\Sigma^{\lambda,\mathrm{M}}(\tau-\bar{\tau})\mathcal{G}^{\lambda,\mathrm{M}}(\bar{\tau}) = \delta(\tau) \tag{27}$$

for the grand-canonical version of the Dyson equation and

$$(-\partial_\tau - h)\mathcal{G}^{\mathrm{M}}(\tau) - \int_0^\tau d\bar{\tau}\Sigma^{\mathrm{M}}(\tau-\bar{\tau})\mathcal{G}^{\mathrm{M}}(\bar{\tau}) = 0 \tag{28}$$

for the projected Dyson equation. While Eq. (27) is a boundary value problem and must be solved by Fourier transformation [$\mathcal{G}^{\lambda,\mathrm{M}}(\beta) = \pm\mathcal{G}^{\lambda,\mathrm{M}}(0^-)$ for bosons or fermions], the projected Eq. (28) is an initial value problem [$\mathcal{G}^{\mathrm{M}}(0) = -1$], which is most efficiently solved in the imaginary time domain.

### C. Diagram rules for the pseudoparticle self-energy

Because the local part of the pseudoparticle action in Eq. (10) is quadratic, a diagrammatic expansion of pseudoparticle Green's functions and self-energies in terms of $\Lambda$ can be derived from the standard rules for general quartic interaction terms (see, e.g., Ref. 49). Each diagram for $\Sigma^{\lambda}$ contains one sequence of pseudoparticle propagators that connect the two external vertices (the "backbone") and possibly additional loops of propagator lines, e.g., renormalizations of the hybridization function [Fig. 2(a)]. To leading order in $\zeta$, the backbone $\mathcal{G}^{\lambda}(t,t_n)\cdots\mathcal{G}^{\lambda}(t_2,t_1)\mathcal{G}^{\lambda}(t_1,t')$ is given by $k_{\lambda}(t,t')\mathcal{G}(t,t_n)\cdots\mathcal{G}(t_2,t_1)\mathcal{G}(t_1,t')$ if $t_1,\ldots,t_n$ are in cyclic order along $\mathcal{C}$, and smaller by $\mathcal{O}(\zeta)$ if the vertices are not ordered [cf. Eq. (18)]. Each closed loop of pseudoparticle propagators contributes an additional exponentially small factor $\zeta$. Thus the diagram rules for the projected self-energy $\Sigma(t,t') = \Sigma^{\lambda}(t,t')/k_{\lambda}(t,t')$ can be obtained from the diagram rules for $\Sigma^{\lambda}$ by (i), replacing pseudoparticle propagators defined in Eq. (13) by projected propagators defined in Eq. (15), (ii), discarding diagrams with closed loops, and (iii), requiring vertices along the backbone to be in cyclic order along $\mathcal{C}$.

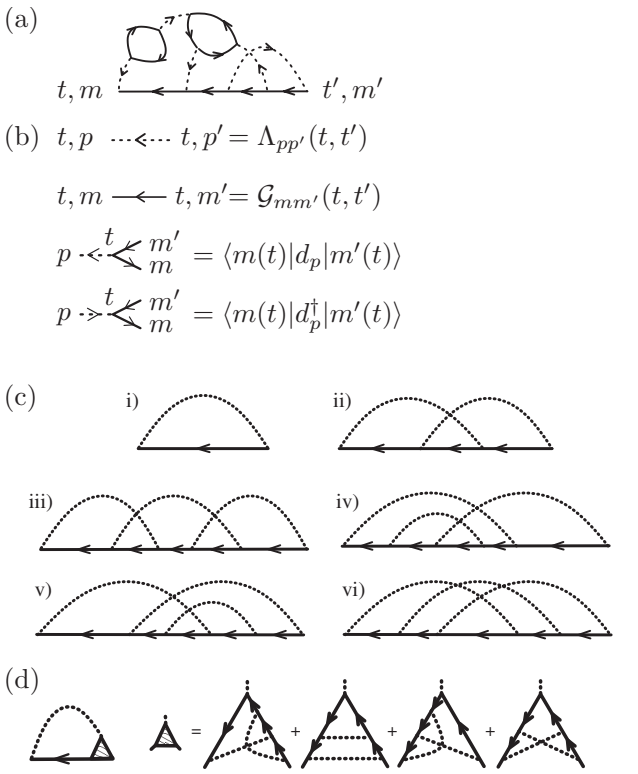


FIG. 2. (a) A fifth-order contribution to the self-energy $\Sigma^{\lambda}_{mm'}(t,t')$, consisting of Green's functions $\mathcal{G}^{\lambda}_0$ (solid lines) and hybridization functions $\Lambda$ (dotted lines). (b) Building blocks of the diagrams in the hybridization expansion. The pseudoparticle line (solid line) corresponds to the interacting propagator $\mathcal{G}$ in skeleton expansions and to $\mathcal{G}_0$ otherwise. (c) All diagrams for $\Sigma^{\mathrm{scel}}[\mathcal{G},\Lambda]$ up to third order. In the topologies indicated, the hybridization line can point in any direction, which gives 2, 4, and $4\times 8$ diagrams in first, second, and third order, respectively. (d) Factorization of third-order diagrams [(iii)–(vi) in (c)] by separating out the vertex part.

For completeness we summarize the final rules for constructing the projected self-energy $\Sigma(t,t')$: (i) the $n$th-order contribution to $\Sigma(t,t')$ is given by all diagrams consisting of $2n$ three-leg vertices [Fig. 2(b)] at times $t_0 = t'$, $t_1,\ldots,t_{2n} = t$, of which $n$ correspond to annihilation operators $d$ (outgoing hybridization line), and $n$ correspond to $d^{\dagger}$ (ingoing hybridization line). The vertices are labeled according to Fig. 2(b). They are connected by one sequence of pseudoparticle lines (solid lines, pointing from $t'$ to $t$), and $n$ hybridization lines (dotted lines) in all possible ways such that the diagram cannot be separated into two parts by cutting only one line. (ii) Sum over all internal flavor indices, and integrate over the internal times $t_1,\ldots,t_{2n-1}$, respecting the cyclic order $t' < t_1 < \cdots < t$. (iii) Because exactly one fermionic pseudoparticle operator is attached to each end of a hybridization line, the sign of the diagram is $(-1)^{s+f}$, where $s$ is the number of crossing of hybridization lines, and $f$ is the number of hybridization lines that point opposite to the direction

of the backbone. (iv) An overall factor $i^n$ must be added.

The diagrammatic expansion for $\Sigma$ can be resummed by replacing bare propagators with interacting propagators $\mathcal{G}$ and in turn taking into account only skeleton diagrams, i.e., diagrams in which internal propagator lines have no self-energy insertions. Truncation of the skeleton series $\Sigma^{\mathrm{scel}}[\mathcal{G},\Lambda]$ at finite order leads to conserving approximations[50] because in this case the approximate self-energy functional can be derived from an approximation to the Luttinger-Ward functional.[51] In particular, this fact ensures the conservation of the pseudoparticle number in Eq. (7), which is crucial in order to obtain a meaningful approximation scheme for nonequilibrium situations. To leading order in $\zeta$, the conservation of $\langle Q\rangle_\lambda$ implies

$$\tilde{Q} \equiv \lim_{\lambda\to\infty} \frac{\langle Q\rangle_\lambda}{\zeta} = i\sum_m (-1)^m \mathcal{G}_{mm}(t,t^+), \tag{29}$$

$$= -\sum_m \mathcal{G}^{\mathrm{M}}_{mm}(\beta), \tag{30}$$

where $t^+$ is infinitesimally later on $\mathcal{C}$ than $t$, and $(-1)^m=\pm 1$ if $m$ corresponds to Bose or Fermi particles, respectively. These relations provide a good check for the numerical implementation.

All skeleton diagrams up to third order are displayed in Fig. 2(c). The self-consistent strong-coupling expansion has been proposed long ago[30–32]as an approximate solution for the Anderson impurity model. Kuramoto[32] coined the term noncrossing approximation for the lowest order, i.e., keeping only the first diagram in Fig. 2(c). In the present work we use the skeleton series up to third order as an impurity solver within nonequilibrium DMFT and compare the results to CTQMC (Sec. IV).

### D. Diagram rules for the impurity Green's function

In general, expressions for observables in the impurity model can be derived from the grand potential $\Omega_\lambda=-\beta^{-1}\log \mathrm{Tr}[\zeta^Q T_{\mathcal{C}} e^{\tilde{\mathcal{S}}_{\mathrm{imp}}}]$. Because diagrams for the correction $\Delta\Omega_\lambda=\Omega_\lambda-\Omega_\lambda(\Lambda=0)$ contain at least one closed loop of pseudoparticle lines, $\Delta\Omega_\lambda$ is proportional to $\zeta$ for $\lambda\to\infty$. The leading order in $\zeta$

$$\Omega = \lim_{\lambda\to\infty} \frac{-1}{\zeta\beta} \log \mathrm{Tr}[\zeta^Q T_{\mathcal{C}} e^{\tilde{\mathcal{S}}_{\mathrm{imp}}}] \tag{31}$$

is obtained by adding to the local contribution $\Omega(\Lambda=0)$ all diagrams of $\Omega_\lambda$ which contain only one loop, in which $\mathcal{G}^\lambda$ is replaced by $\mathcal{G}$, and where integrals over the internal vertices are restricted such that the vertices are in cyclic order. (See the analogous argument for $\Sigma$ in Sec. III C.)

Using Eq. (14), the impurity Green's function in Eq. (3) is given by $G(t,t')=\lim_{\lambda\to\infty} G^\lambda(t,t')/\langle Q\rangle_\lambda$, where $G^\lambda_{pp'}(t,t')=-i\langle T_{\mathcal{C}} \tilde{d}_p(t)\tilde{d}^\dagger_{p'}(t')\rangle_\lambda$. It can thus be obtained from the derivative [cf. Eqs. (9), (10), (29), and (31)]

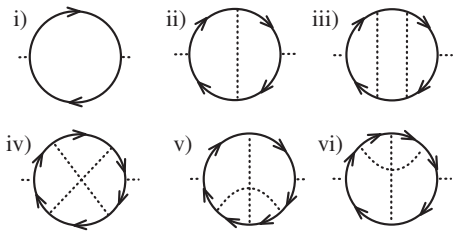


FIG. 3. All diagrams for $G^{\mathrm{scel}}[\mathcal{G},\Lambda]$ in first order [diagram (i)], second-order [diagram (ii)], and third-order [diagram (iii)–(vi)]. Internal hybridization lines can point in any direction, which gives 1, 2, and $4\times 4$ diagrams in first, second, and third order, respectively.

$$G_{pp'}(t,t') = \frac{\beta}{\tilde{Q}} \frac{\delta\Omega}{\delta\Lambda_{p'p}(t',t)}. \tag{32}$$

Diagrams for $G(t,t')$ (in terms of the projected pseudoparticle Green's functions) are therefore constructed by removing one hybridization line from the diagrams for $\Omega$ (Fig. 3). Note that a diagram for $\Omega$ generally has a symmetry factor $1/S\neq 1$, where $S$ is the number of topologically equivalent ways to label the vertices. The symmetry factor disappears in the expansion of $G$ because for a diagram with symmetry factor $1/S$ there are $S$ ways to remove a hybridization line which lead to the same diagram for $G$. The series for $G$ can thus be resummed in the same way as the series for $\Sigma$, i.e., by keeping only skeleton diagrams for $G$, and replacing $\mathcal{G}_0$ with $\mathcal{G}$. Equation (32) then holds also for the skeleton expansion

$$G^{\mathrm{scel}}_{pp'}[\mathcal{G},\Lambda](t,t') = \frac{\beta}{\tilde{Q}} \frac{\delta\Omega^{\mathrm{scel}}[\mathcal{G},\Lambda]}{\delta\Lambda_{p'p}(t',t)}, \tag{33}$$

where $\Omega^{\mathrm{scel}}[G,\Lambda]$ is the Luttinger Ward functional, i.e., the skeleton expansion for $\Omega$ in terms of the fully interacting (projected) propagators $\mathcal{G}$. To design an approximation for $G^{\mathrm{scel}}[\mathcal{G},\Lambda]$ which is consistent with a given approximation of $\Sigma$ one must truncate both $\Omega^{\mathrm{scel}}[\mathcal{G},\Lambda]$ and $\Sigma^{\mathrm{scel}}[\mathcal{G},\Lambda]$ at the same order.

The final rules for $G^{\mathrm{scel}}[\mathcal{G},\Lambda]$ read: the $n$th-order contribution consists of a loop of projected pseudoparticle propagator lines [Fig. 2(b)] which connects $2n$ vertices ($n$ annihilation operators, $n$ creation operators). One $d$-vertex (time $t$, $\Lambda$ line labeled $p$) and one $d^\dagger$ vertex (time $t'$, $\Lambda$-line labeled $p'$) are external vertices. The internal vertices are connected by hybridization lines such that no internal line has a self-energy insertion. Sum over all internal flavor indices and integrate over internal (contour) time variables respecting the cyclic order of $t_1,\ldots,t_{2n}$ along the contour. Add a prefactor $i^n$. To determine the sign of a diagram $D$, reinsert the $\Lambda$ line between the external vertices. This recovers the diagram $D'$ in the expansion of $\Omega$ from which the diagram $D$ is derived. The sign $\kappa_D$ of $D$ is given by the sign of $D'$, i.e., $\kappa_D=(-1)^{s+f}$, where $s$ is the number of crossings of hybridization lines, and $f$ is the number of hybridization lines that go in opposite direction to the string of pseudoparticle lines that is obtained if the loop is cut at an arbitrary fermionic propagator line. All skeleton diagrams for $G$ up to third order are shown in Fig. 3.

### E. Numerical implementation

Before presenting benchmark results for the self-consistent hybridization expansion, we would like to make some remarks on the numerical implementation. First of all, we note that the number of possible labelings for the internal flavor indices is usually quite restricted. As an example, consider the single-impurity Anderson model with the four basis states $|0\rangle$, $|\sigma\rangle=d_\sigma^\dagger|0\rangle$, and $|\uparrow\downarrow\rangle=d_\downarrow^\dagger d_\uparrow^\dagger|0\rangle$, $H_{\rm loc}=Ud_\uparrow^\dagger d_\uparrow d_\downarrow^\dagger d_\downarrow-\mu(d_\uparrow^\dagger d_\uparrow+d_\downarrow^\dagger d_\downarrow)$, and $S_{\rm hyb}=-i\int_{\mathcal{C}}dtdt'\Sigma_\sigma d_\sigma^\dagger(t)\Lambda_\sigma(t,t')d_\sigma(t')$. The matrix elements in Eq. (9c) are nonzero only for the combinations $F^\sigma_{\sigma,0}=1$ and $F^{\bar\sigma}_{\uparrow\downarrow,\sigma}=\sigma$. Furthermore, Green's functions are diagonal in pseudoparticle flavor, because both the interaction part and the hybridization function are diagonal in the occupation number basis. The second-order diagram for $\Sigma_{mm}(t,t')$, e.g., then only allows eight possible labelings for the three internal Green's function lines, which are $(\uparrow,0,\downarrow)$ and $(\downarrow,0,\uparrow)$ for $m=\uparrow\downarrow$, $(0,\bar\sigma,\uparrow\downarrow)$ and $(\uparrow\downarrow,\bar\sigma,0)$ for $m=\sigma$, and $(\uparrow,\uparrow\downarrow,\downarrow)$ and $(\downarrow,\uparrow\downarrow,\uparrow)$ for $m=0$.

To obtain a self-consistent solution, the hybridization expansion is evaluated by iteratively solving the Dyson equation for $\mathcal{G}(t,t')$ [Eq. (26)], and evaluating the integral expressions for $\Sigma(t,t')$. However, the real-time version of the expansion can easily be implemented in a slightly simpler way that exploits the causal structure of the equations. If we have computed $\mathcal{G}(t,t')$ for $\mathrm{Re}(t)$, $\mathrm{Re}(t')\le t_{\rm max}$, then $\mathcal{G}(t_{\rm max}+\Delta t,t')$ and $\mathcal{G}(t,t_{\rm max}+\Delta t)$ can be obtained from the above-mentioned iteration in only one or two steps by starting from a polynomial extrapolation of $\mathcal{G}(t,t')$. This amounts to a stepwise propagation of the solution on the imaginary branch of $\mathcal{C}$ to real times.

The numerical effort of the evaluation of diagrams is mainly determined by the contour integrals over the internal vertices. Using Monte Carlo for the evaluation of the integrals for higher order diagrams will lead to a sign problem. We use a quadrature formula for the integrals which is based on equidistant discretization of the contour $\mathcal{C}$. The $n$th-order diagrams have $2n-2$ internal integrals [cf. Figs. 2(c) and 3], which have to be evaluated for each combination of the two external time variables. (Nonequilibrium correlation functions depend on both time arguments separately). This seems to imply that the numerical effort for the evaluation of $\Sigma$ and $G$ scales with the number $N$ of mesh points like $N^2$, $N^4$, and $N^6$ for first, second and third order, respectively. (The effort for the solution of the Dyson equation, which is essentially a matrix inversion on $\mathcal{C}$, scales as $N^3$.) However, one can reduce the effort for the evaluation of the third-order diagrams to $N^5$ by factorizing out a vertex part $\tilde F$ with two internal integrals and three external variables [Fig. 2(d)]; $\Sigma$ and $G$ can then be computed from $\tilde F$ with only two additional integrals. Since $\tilde F$ does not have to be stored in memory, this way of evaluation is more efficient than performing four internal integrals.

## IV. COMPARISON TO CTQMC

### A. Interaction quench in the Hubbard model

Nonequilibrium DMFT for the interaction quench in the Hubbard model provides a perfect framework to benchmark the perturbative impurity solver. The Hubbard Hamiltonian

$$H(t)=\sum_{ij\sigma}V_{ij}c_{i\sigma}^\dagger c_{j\sigma}+U(t)\sum_i\left(n_{i\uparrow}-\frac{1}{2}\right)\left(n_{i\downarrow}-\frac{1}{2}\right) \quad (34)$$

describes fermions of spin one half which hop on a lattice with hopping amplitude $V_{ij}$ and interact with a repulsion energy $U$ on each site. To perform an interaction quench, the system is prepared in a thermal equilibrium state at temperature $T=1/\beta$ and interaction $U(t<0)=U_0$ for times $t<0$, and the interaction is suddenly switched to a new value $U(t>0)=U$ at $t=0$.

The DMFT equations for the interaction quench have been explained in detail in Refs. 18 and 19. In the following we assume that the hopping matrix $V_{ij}$ has a semielliptic local density of states

$$\rho(\epsilon)=\sqrt{4-(\epsilon/V)^2}/2\pi V \quad (35)$$

(with half-bandwith $2V$) and we focus on the paramagnetic state at half-filling. DMFT then reduces to a set of two self-consistent equations:[18,19] (i) the local lattice Green's function in Eq. (3) must be determined from the single-site action in Eq. (1), where the index $p$ now labels spin $\sigma=\uparrow,\downarrow$, and the local Hamiltonian is given by

$$H_{\rm loc}(t)=U(t)\sum_i\left(n_{i\uparrow}-\frac{1}{2}\right)\left(n_{i\downarrow}-\frac{1}{2}\right). \quad (36)$$

(ii) The hybridization function is determined by the self-consistency[52]

$$\Lambda_\sigma(t,t')=V^2G_\sigma(t,t'). \quad (37)$$

The hopping $V=1$ is used as an energy unit and times are measured in units of the inverse hopping ($\hbar=1$).

Below we solve these DMFT equations by means of the self-consistent hybridization expansion and compare to results from CTQMC.[18,19] In particular, we focus on the time evolution and the thermal equilibrium value of the double occupancy per site, $d(t)=\langle n_{i\uparrow}n_{i\downarrow}\rangle$, which is a local observable and can thus be measured directly in the impurity model, i.e.,

$$d(t)=i\tilde Q^{-1}\mathcal{G}_{\uparrow\downarrow}(t,t^+), \quad (38)$$

where $\mathcal{G}_{\uparrow\downarrow}$ is the propagator for doubly occupied sites and $t^+$ is infinitesimally later on $\mathcal{C}$ than $t$.

### B. Initial equilibrium state

Figure 4 shows the double occupancy $d_{eq}(\beta,U)$ in the thermal equilibrium state at interaction $U$ and inverse temperature $\beta$. At large enough temperature, $d_{eq}(T,U)$ decreases smoothly as a function of $U$ [Fig. 4(a)]. As $T$ is lowered, the curves bend strongly around $U=4.5$ [Fig. 4(b)], indicating a narrow crossover between metallic and insulating behavior. Below a critical temperature $T_c$, the transition between metal and insulator becomes a first-order phase transition [Fig. 4(c)]. For the semielliptic density of states, the end point of this Mott transition is located at $U_c=4.7$ and $T_c=0.055$.[53]

In agreement with recent results based on a Monte Carlo sampling around NCA,[40] we find that NCA can reproduce

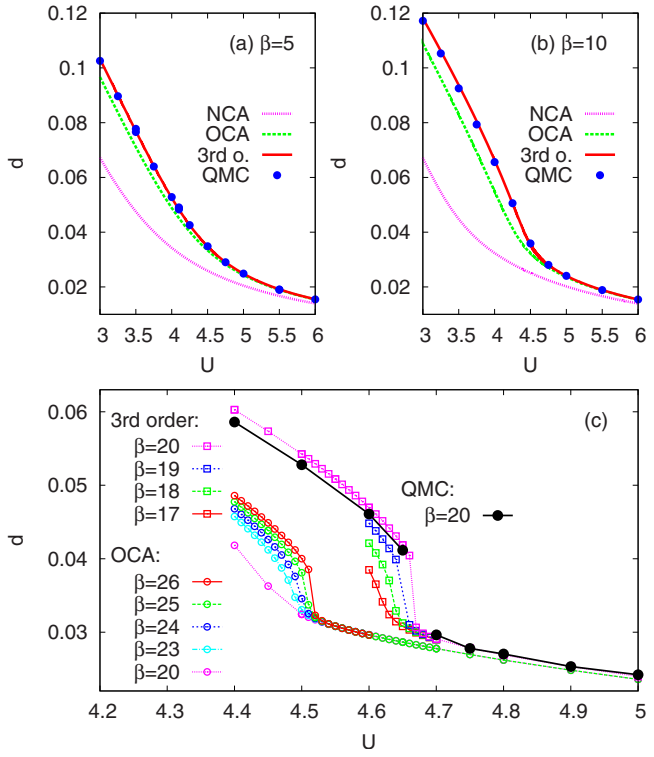


FIG. 4. (Color online) Double occupancy $d_{eq}(\beta,U)$ in the thermal equilibrium state. The impurity solver is either CTQMC, or the self-consistent hybridization expansion up to first (NCA), second (OCA), and third order. (a) $\beta=5$. (b) $\beta=10$. (c) $\beta$ close to the critical temperature $T_c$ of the first-order metal-insulator transition.

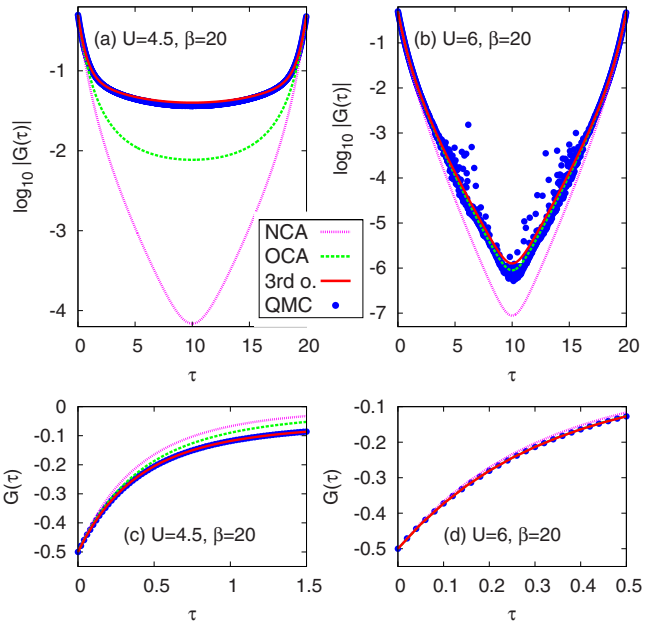


FIG. 5. (Color online) Matsubara component defined in Eq. (5) of the local Green's function $G_\sigma(\tau)$ [Eq. (3)], which is independent of $\sigma$ in the paramagnetic phase. The impurity solver is either CTQMC, or the self-consistent hybridization expansion up to first (NCA), second (OCA), and third order. (a) $U=4.5$, $\beta=20$ (crossover regime). (b) $U=6$, $\beta=20$ (insulating phase). Note that the CTQMC results in the insulating phase are only accurate for values larger than the "noise floor" of about $10^{-3}$. Panels (c) and (d) show the same data as (a) and (b), respectively, but plotted for small $\tau$ on a linear scale.

the CTQMC results only deep in the insulating phase. However, already the lowest order correction to NCA, i.e., OCA, very well accounts for the nonlinear behavior of $d_{eq}(U,T)$ in the crossover regime, and the third order in the self-consistent hybridization expansion almost quantitatively recovers the CTQMC results even close to the critical point [Fig. 4(c)]. The location of the critical end point in the phase diagram is in good agreement with previous QMC results:[53] if we estimate $T_c$ from the smallest $\beta$ for which we can detect hysteretic behavior in $d_{eq}(\beta,U)$ (this gives actually a lower bound for $T_c$), we find $T_c > 1/19 \approx 0.052$ for the third order and $T_c > 1/26 \approx 0.038$ for OCA [Fig. 4(c)]. NCA, on the other hand, does not display singular behavior in this parameter regime. As usual, the convergence of the DMFT equations slows down close to the critical point, and it is thus hard to get precise numbers for $T_c$ and $U_c$.

The order-by-order convergence of the self-consistent hybridization expansion is also evident from the local Green's function $G(\tau)$, both in the crossover regime [Fig. 5(a)] and in the insulating phase [Fig. 5(b)]. From the value $G(\beta/2)$ one can see that NCA overestimates the insulating nature of the solution. This fact reflects a well known deficiency of NCA: the Kondo temperature $T_K$ for the Anderson model comes out correct within NCA for $U=\infty$ but it is severely underestimated for finite interaction $U$. This problem can be cured by taking into account certain vertex corrections, which correspond to summing up higher order terms in the self-consistent expansion.[38,39] Our results show that the third order is sufficiently accurate in a wide parameter range covering the insulating phase and the crossover regime, even close to the critical point.

Another known deficiency of the NCA is that the Fermi liquid in the Anderson impurity model for $T \ll T_K$ is not correctly described.[37] Because this problem cannot be cured by taking into account finite order diagrams in the hybridization expansion,[39] one would expect that even the third order will yield wrong results in the metallic phase at low-enough temperature. Empirically, we find a slow down of the convergence as the temperature is lowered in the metallic phase and we have not systematically studied the breakdown of the truncated self-consistent hybridization expansion deep in the metallic phase.

### C. Time evolution of the double occupancy

To test the accuracy of the strong-coupling expansion for nonequilibrium problems we compute the time evolution of the double occupancy after an interaction quench. Due to the dynamical sign problem, weak-coupling CTQMC calculations for interacting initial states[19] can be performed only to relatively short times $t_{\max}$, which mainly depend on the final interaction $U(t>0)$. However, for those $t_{\max}$ which are accessible with CTQMC, the comparison with the strong-coupling expansion reveals a similar trend as for thermal equilibrium states (Fig. 6): for quenches from the crossover

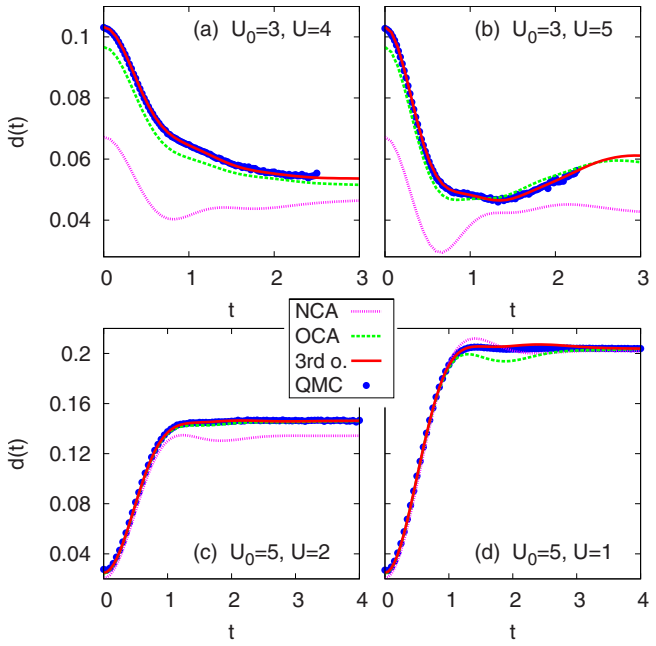


FIG. 6. (Color online) Double occupancy $d(t)$ after an interaction quench from $U_0$ to $U$. [(a) and (b)] Initial states in the crossover regime [$U_0=3$, $\beta=5$], [(c) and (d)] Initial states in the insulating phase [$U_0=5$, $\beta=5$].

region to larger interaction both the initial state and the time evolution is not correctly described within NCA, whereas OCA is more reliable, and the third-order calculation recovers the CTQMC results almost quantitatively [Figs. 6(a) and 6(b)]. While Figs. 6(a) and 6(b) show the longest times accessible with CTQMC, the OCA and the third-order calculations can be carried to substantially longer times. For a quench from the insulating phase to smaller interaction, NCA is better suited to describe the initial state but differences to CTQMC become more pronounced during the time evolution [Figs. 6(c) and 6(d)].

## V. MODULATION SPECTROSCOPY ON THE MOTT INSULATING PHASE

### A. Introduction

To illustrate the capability of the approach, we are now going to present an application of the strong-coupling hybridization expansion in a parameter regime where the weak-coupling CTQMC approach would be numerically too expensive. Our aim is to compute the response of the double occupancy in the Mott insulator to a time-dependent change in the interaction $U$ or the hopping amplitude $V$. Such an experiment, with a periodic change in the hopping, was originally proposed by Kollath *et al.*[20] as a new type of spectroscopy for ultracold gases in optical lattices without direct analogon in solid state physics. In the meantime, the technique has been used as an experimental probe for the detection of the Mott insulating phase of ultracold $^{40}$K atoms in an optical lattice.[21]

In the experiments, the hopping amplitude $V(t)=V_0[1+\alpha\cos(\omega t)]$ is modulated sinusodially over several tens of periods $2\pi/\omega$.[21,22] Apart from an oscillating component $d_{osc}(t)$ with zero time-average, the double occupancy $d(t)$ rises linearly in time for small times and saturates within a time scale $\tau_{sat}$. In the Mott insulating phase, the modulation spectrum, i.e., the magnitude of the response as a function of the frequency, has a peak when $\omega$ is approximately at resonance with the energy $U$ that is needed for the creation of a doublon-holon pair, and a gap at $\omega=0$.[20,54]

Because the modulation strength can be quite large, many aspects of those experiments can only be understood by means of a nonequilibrium formalism. This is certainly the case for the saturation time $\tau_{sat}$ (Ref. 55) and for the nonequilibrium quasisteady (time-periodic) state which the system is in once it has saturated. Even when averaged over time, such a state might have properties which do not resemble any thermal equilibrium state of the system. Nonequilibrium DMFT can be used to resolve some of these issues. In the following, we demonstrate that DMFT yields a modulation spectrum which is in agreement with a recent investigation based on slave-boson mean-field theory[54] and similar to what has been obtained in time-dependent density-matrix renormalization group calculations for the one-dimensional Hubbard model.[20] Furthermore, we will show that a slightly different modulation procedure, namely, a quench of the hopping or the interaction by a few percent, provides another probe which is sensitive to the Mott transition and the metal-insulator crossover at higher temperatures.

### B. Periodic modulation of $U$

In the following we consider the Hubbard model in Eq. (34) with a time-dependent interaction

$$U(t>0)=U_0[1+\alpha\cos(\omega t)], \tag{39}$$

where $\alpha$ is the relative modulation strength ($\alpha<1$). For times $t<0$, the system is prepared in an equilibrium state at interaction $U(t<0)=U_0$ and temperature $T=1/\beta$. The model is treated within nonequilibrium DMFT, assuming a semielliptic density of states in Eq. (35), such that the self-consistency is given by Eq. (37). The energy scale is fixed by the quarter bandwidth $V=1$. Because we will restrict the investigation to insulating states and to the crossover regime, we will mainly use OCA as an impurity solver.

Experimentally, the hopping is more easily tunable than the interaction because the former is strongly affected by a change of the optical lattice depth. Our description in Eq. (39) is nevertheless justified because modulation of $U$ and $V$ are equivalent from a theoretical point of view, and only the ratio $U/V$ matters. The Hubbard model $H(t)$ with time-dependent interaction in Eq. (39) and time-independent hopping $V_0$ can be mapped onto an equivalent model with time-independent interaction $U_0$ and periodic hopping $V(t')=V_0/\{1+\alpha\cos[\omega t(t')]\}$, where $t(t')$ is the inverse of the transformation $t'(t)=t+\alpha\sin(\omega t)/\omega$. To lowest order in $\alpha$, modulation of $U(t)=U_0[1+\alpha\cos(\omega t)]$ and $V(t')=V_0[1-\alpha\cos(\omega t')]$ are thus equivalent, although higher harmonic terms $\propto\alpha^n\cos(n\omega t')$ appear in $V(t')$ for large $\alpha$. The equivalence can be established by a simple change of time variables in the time-evolution operator

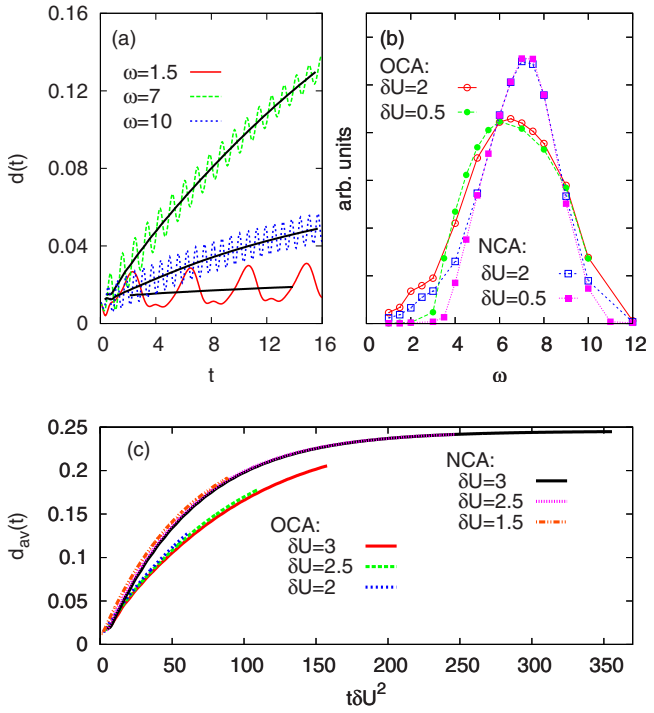


FIG. 7. (Color online) (a) Double occupancy $d(t)$ during a periodic modulation of the interaction around $U_0=7$ ($\beta=10$, $\delta U=\alpha U_0=2$). The frequency is below the resonance peak ($\omega=1.5$), close to the resonance ($\omega=7$), and above the resonance ($\omega=10$). Bold solid lines indicate the average $d_{av}(t)$ over one period $[t-\pi/\omega, t+\pi/\omega]$. OCA was used as an impurity solver. (b) Modulation spectrum for $U_0=7$ and $\beta=10$, using either NCA or OCA as an impurity solver: For large amplitude $\delta U=2$, the data have been obtained from $d_{av}(t_0)$ at given time $t_0=10$ (open symbols); for small amplitudes $\delta U=0.5$, the slope $(d/dt)d_{av}(t)$ in the interval $8<t<10$ is plotted (full symbols). The curves have been scaled with a constant factor to match their peak heights. (c) Averaged double occupancy $d_{av}(t)$ at $U_0=7$ for various modulation amplitudes $\delta U=\alpha U_0$, plotted against $t\delta U^2$. The three curves labeled NCA almost fall on top of each other.

$\mathcal{U}(t,0)=T_t \exp[-i\int_0^t d\bar{t} H(\bar{t})]$ from $t$ to $t'$, which yields $\mathcal{U}'(t',0)=\mathcal{U}(t(t'),0)$, where $\mathcal{U}'(t',0)$ is the time-evolution operator for the model $H'(t')$ with periodically modulated hopping $V(t')$.

The typical time-evolution of the double occupancy $d(t)$ during a periodic modulation of $U$ is displayed in Fig. 7(a). The effect of the modulation vanishes for $\omega\to 0$ and is largest close to $\omega\approx U$. The anharmonic behavior in $d(t)$ for small frequencies $\omega$ is due to a rather large amplitude $\delta U\equiv\alpha U_0$. After removing the oscillating component $d_{osc}(t)$ by taking an average $d_{av}(t)=\int_{t-\pi/2}^{t+\pi/2} dt' d(t')$ over one period $\tau=2\pi/\omega$, one can clearly identify an initial linear increase with a slope $\Gamma(\omega)$, followed by a trend toward saturation at longer times.

The rate $\Gamma(\omega)$ can be obtained from second order time-dependent perturbation theory, i.e., $\Gamma\propto\alpha^2$ for $\alpha\ll 1$.[20,54] (Linear response yields only an oscillating contribution.) Since the resulting Fermi's golden rule expression for $\Gamma$ depends only on the equilibrium state of the system at $U=U_0$,[54] it would be best to measure $\Gamma(\omega)$ directly in the limit $\alpha\to 0$. To extract the slope $\Gamma(\omega)$, one has to go to small amplitudes $\alpha$ anyway because only then does the linear region extend over many oscillation periods. On the other hand, experiments are performed at quite large $\alpha$ in order to obtain a good signal to noise ratio and the magnitude of the response is defined by the value of the double occupancy $d_{av}(t)$ at given time $t_0$. Usually, $t_0$ is chosen so large that $d_{av}(t)$ is no longer linearly increasing at $t=t_0$.

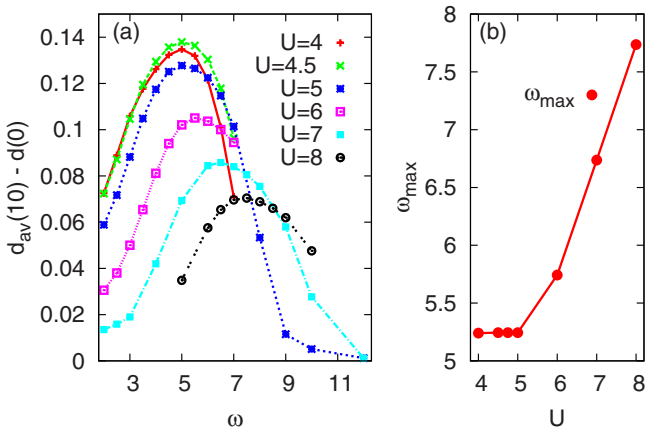


FIG. 8. (Color online) (a) Modulation spectrum at $\beta=10$ and various interactions $U_0$, obtained from the increase $d_{av}(t_0)-d(0)$ at $t_0=10$ ($\delta U=2$). (b) Location of the maximum $\omega_{\max}$ of the spectra in (a), plotted against $U_0$.

In Fig. 7(b) we compare two ways to quantify the response: either, (i) the increase of the double occupancy $d_{av}(t_0)-d(0)$ is measured at a given time $t_0$ for large modulation amplitudes as a function of frequency, or (ii) the slope $\Gamma(\omega)$ is obtained from a linear fit to the initial increase for smaller amplitudes $\alpha$. Both approaches give a modulation spectrum with a peak at $\omega\approx U$ and a gap at $\omega=0$. Similar to the findings of the previous section, the NCA solution slightly overestimates the insulating nature of the solution compared to the more reliable OCA. Like in the one-dimensional case,[20] our data show that the location of the peak at $\omega\approx U$ is not considerably shifted if the measurement is no longer performed at $\alpha\ll 1$. The gap, on the other hand, is most reliably extracted from the second approach (ii). In the following we will only focus on the peak and not investigate the low-frequency weight in detail.

Figure 8(a) displays the peak in the modulation spectrum for various values of $U_0$. For the semielliptic density of states, the first-order phase transition line terminates at $U_c\approx 4.7$ and $T_c\approx 0.055$,[53] and the zero-temperature transition is located at $U_{c2}\approx 6$. Hence the data in Fig. 8, which are computed at $T=0.1$, correspond to a cut through the crossover region of the metal-insulator phase diagram. The peak in the modulation spectrum is clearly visible all throughout the insulating phase and the crossover regime between metal and insulator. Its position $\omega_{\max}(U_0)$ scales linearly with $U_0$ in the insulating phase [Fig. 8(b)] while in the crossover regime we find only a weak dependence on $U_0$. This finding is in good agreement with results for $\Gamma(\omega)$ from slave-boson mean-field theory,[54] where peaks around $\omega\approx U$ and $\omega\approx U_{c2}$ are predicted for the insulating phase and the metallic phase, respectively. In the slave-boson approach, these spectral features arise from excitations between the Hubbard bands in

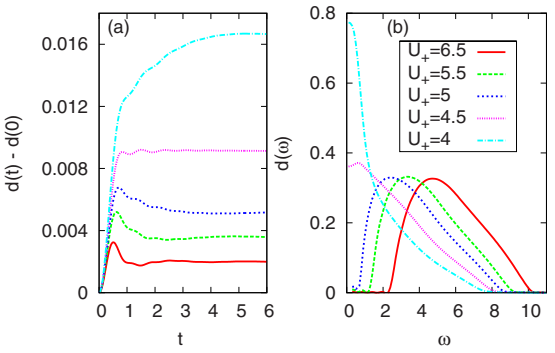


FIG. 9. (Color online) (a) The double occupancy after quenches from $U=U_0$ to $U=U_0-\delta U$, with $\delta U=0.5$, $\beta=10$, and $U_0=7,6,5.6,5,4.5$. OCA has been used as an impurity solver. (b) Fourier transform in Eq. (40) of the data in (a).

the insulator and between pre-formed Hubbard bands in the metallic phase.

Since our calculation is performed at temperatures above $T_c$ and the preformed Hubbard bands shift with $U$, the almost kinklike $\omega_{\max}(U_0)$ seems very remarkable. It should be investigated whether the third order in the expansion leads to a smoothening of this feature. This will require quite some numerical effort (although it is still feasible using small-scale parallelization) and it is thus left to future work, which should involve a more realistic setup.

Another interesting topic is the saturation of $d_{av}(t)$ at large times.[55] A scaling of the time axis with $\alpha^2$ indicates that the saturation time $\tau_{sat}$ behaves like $\tau_{sat}\propto\alpha^{-2}$ in the insulating phase for frequencies $\omega=U$ [Fig. 7(c)] while the saturation value $d_{av}(t\to\infty)$ does not depend sensitively on $\delta U$. However, due to the long times needed to reach saturation at small $\delta U$, this result has so far only been computed using NCA as an impurity solver, which is reliable only deep in the insulating phase. A dependence $\tau_{sat}\propto\alpha^{-2}$ would be consistent with an incoherent pumping mechanism into a doublon-holon continuum.[55]

### C. Quenchlike modulation of $U$

Modulation spectroscopy for the double occupancy is, in principle, not restricted to the periodic modulation Eq. (39). In particular, a small interaction quench from $U(t<0)=U_0$ to $U(t>0)=U_0+\delta U$, or an equivalent quench of the hopping, can be viewed as a modulation experiment as well. In order to extract a frequency-dependent response signal, we define the Fourier transform

$$\tilde{d}(\omega)=\mathrm{Re}\int_0^{t_{\max}}dt e^{i\omega t}[d(t)-d(t_{\max})], \tag{40}$$

where $t_{\max}$ is the maximum time reached in the simulation and $d(t)=(1/Z)\mathrm{Tr}[e^{-\beta H_0}e^{iHt}de^{-iHt}]$ is the time-dependent double occupancy. Using first-order perturbation theory one obtains

$$\tilde{d}(\omega)=\omega^{-1}\ \mathrm{Im}\ \tilde{\chi}(\omega)+\mathcal{O}[(\delta U\beta)^2], \tag{41}$$

where $\tilde{\chi}(\omega)=\int_0^\infty ds e^{i(\omega+i0)s}\chi(s)$ is the Fourier transform of linear response function

$$\chi(s)=-i\frac{1}{Z}\mathrm{Tr}(e^{-\beta H}[e^{iHs}de^{-iHs},d]) \tag{42}$$

of the final Hamiltonian $H(t>0)$. Equation (41) holds for $\omega\neq 0$ and $t_{\max}\to\infty$, while evaluation of $\tilde{d}(\omega)$ at $t_{\max}<0$ corresponds to a broadening of $\chi(\omega)$ on the scale $1/t_{\max}$. The time-independent expansion parameter $\beta\delta U$ in Eq. (41) is obtained by performing a perturbation expansion of the initial state density matrix $\exp[-\beta H(t<0)t]$ instead of the time-evolution operator $\exp[-iH(t>0)t]$.

In principle, $\chi(\omega)$ could be computed directly from equilibrium DMFT. However, the equilibrium imaginary time formalism requires an analytical continuation while the nonequilibrium calculation gives direct access to frequency or time-dependent quantities. Furthermore, in an experiment the values of $U$ would have to be changed by at least a few percent, such that it is unclear whether Eq. (41) is still appropriate to describe the response.

After an interaction quench from the noninteracting ground state to the insulating phase in the Hubbard model, the double occupancy $d(t)$ relaxes through a series of oscillations at approximate frequency $U$,[18] which correspond to the well-known collapse and revival oscillations in the limit $U\gg V$.[6] Similar oscillations become visible after small quenches within the insulating phase ($U_+=6.5,5.5,5$ in Fig. 9); their Fourier transform leads to a broad peak around $\omega\approx U$ [Fig. 9(b)]. The series of quenches displayed in Fig. 9 corresponds to a scan through the phase diagram at constant temperature $T=0.1$ above the critical temperature of the Mott transition. A crossover between metallic and insulating behavior is thus expected between $U\approx 4$ and $U\approx 5$. In agreement with this, the gap in $d(\omega)$ at $\omega=0$ disappears between $U=5$ and $U=4.75$. Although the absolute changes of the double occupancy are small, these results suggest that the double occupancy after an interaction quench may be used as probe of the metal-to-insulator crossover in the Hubbard model.

## VI. CONCLUSION

In this paper we have presented a self-consistent diagrammatic strong-coupling expansion on the Keldysh contour, which can be used to solve the Anderson impurity model in rather general nonequilibrium situations. The main purpose of this study was the development of an impurity solver for nonequilibrium DMFT which can cover the regime of large interactions and relatively long times. By comparing results from our strong-coupling expansion to numerically exact weak-coupling CTQMC for the Hubbard model, we found that the strong-coupling expansion is a good candidate to fulfill these requirements: while it fails in the metallic phase and at very low temperatures, and while the first order or noncrossing approximation is correct only deep in the insulating phase, an important correction arises already in the second order (OCA). In the insulating phase and in the crossover regime the latter gives quite reliable results, which can be brought into almost quantitative agreement with CTQMC by going to the third order of the expansion.

Although the numerical effort for the evaluation of the diagrams rises considerably with the expansion order, even

calculations up to third order can be carried to substantially longer times than CTQMC, because the latter suffers from an exponential increase in the computational cost due to the dynamical sign problem. We thus believe that the strong-coupling expansion will allow to extend nonequilibrium DMFT investigations into the parameter regime of rather strong interactions and not too low temperatures which was so far not accessible within weak-coupling CTQMC. It is precisely this parameter regime which is relevant for many experiments with cold atomic gases[21,22] and pump-probe spectroscopy. The broad range of possible applications of DMFT in this field includes the excitation of the Mott insulating phase by a short laser pulse (similar to the experiments in Refs. 3 and 4), the response of the Mott insulator to very strong electrical fields that might lead to a dielectric breakdown,[56] or an extended investigation of the interaction quench in the Hubbard model.[18]

In the last part of the paper we have used the self-consistent hybridization expansion as an impurity solver within nonequilibrium DMFT in order to study the generation of doubly occupied sites in a Mott insulator by a time-dependent variation in the interaction or hopping strength. In agreement with previous investigations,[20,54] the modulation spectrum was found to have a gap at $\omega=0$ and a pronounced maximum at $\omega \approx U$. The maximum persists in the crossover regime but its location is then no longer proportional to $U$. Furthermore, we have studied the double occupancy $d(t)$ as a function of time after small interaction quenches. In the crossover regime, the behavior of $d(t)$ is drastically changing, which is most clearly evidenced by the disappearance of the gap in the Fourier transform of $d(t)$. Although the absolute changes of the double occupancy are small, its time-evolution may thus yield a sensitive probe of the metal-to-insulator crossover in the Hubbard model.

An interesting next step would now be to repeat similar calculations in a more realistic setup, e.g., on a cubic lattice. A careful comparison of results from the self-consistent hybridization expansion up to second and third order and from CTQMC (for small times) will allow to make definite experimental predictions, such as for the modulation spectrum in the insulating phase and the crossover regime, and for the saturation behavior of the double occupancy.

## ACKNOWLEDGMENTS

This work was supported by the Swiss National Science Foundation (Grant No. PP002-118866). CTQMC calculations were run on the Brutus cluster at ETH Zurich, using the ALPS library (Ref. 57).

[1] I. Bloch, J. Dalibard, and W. Zwerger, Rev. Mod. Phys. **80**, 885 (2008).
[2] S. Iwai, M. Ono, A. Maeda, H. Matsuzaki, H. Kishida, H. Okamoto, and Y. Tokura, Phys. Rev. Lett. **91**, 057401 (2003).
[3] L. Perfetti, P. A. Loukakos, M. Lisowski, U. Bovensiepen, H. Berger, S. Biermann, P. S. Cornaglia, A. Georges, and M. Wolf, Phys. Rev. Lett. **97**, 067402 (2006); New J. Phys. **10**, 053019 (2008).
[4] S. Wall, D. Brida, S. Clark, H. Ehrke, D. Jaksch, A. Ardavan, S. Bonora, H. Uemura, Y. Takahashi, T. Hasegawa, H. Okamoto, G. Cerullo, and A. Cavalleri, arXiv:0910.3808 (unpublished).
[5] D. Goldhaber-Gordon, H. Shtrikman, D. Mahalu, D. Abusch-Magder, U. Meirav, and M. A. Kastner, Nature (London) **391**, 156 (1998).
[6] M. Greiner, O. Mandel, T. W. Hänsch, and I. Bloch, Nature (London) **419**, 51 (2002).
[7] T. Kinoshita, T. Wenger, and D. S. Weiss, Nature (London) **440**, 900 (2006).
[8] A. Georges, G. Kotliar, W. Krauth, and M. J. Rozenberg, Rev. Mod. Phys. **68**, 13 (1996).
[9] P. Schmidt and H. Monien, arXiv:cond-mat/0202046 (unpublished); P. Schmidt, Diploma thesis, University of Bonn, 1999.
[10] W. Metzner and D. Vollhardt, Phys. Rev. Lett. **62**, 324 (1989).
[11] G. Kotliar and D. Vollhardt, Phys. Today **57**(3), 53 (2004).
[12] J. K. Freericks, V. M. Turkowski, and V. Zlatić, Phys. Rev. Lett. **97**, 266408 (2006).
[13] J. K. Freericks, Phys. Rev. B **77**, 075109 (2008).
[14] N. Tsuji, T. Oka, and H. Aoki, Phys. Rev. B **78**, 235124 (2008).
[15] N. Tsuji, T. Oka, and H. Aoki, Phys. Rev. Lett. **103**, 047403 (2009).
[16] M. Eckstein and M. Kollar, Phys. Rev. Lett. **100**, 120404 (2008).
[17] M. Eckstein and M. Kollar, New J. Phys. **12**, 055012 (2010).
[18] M. Eckstein, M. Kollar, and P. Werner, Phys. Rev. Lett. **103**, 056403 (2009).
[19] M. Eckstein, M. Kollar, and P. Werner, Phys. Rev. B **81**, 115131 (2010).
[20] C. Kollath, A. Iucci, I. P. McCulloch, and T. Giamarchi, Phys. Rev. A **74**, 041604(R) (2006).
[21] R. Jördens, N. Strohmaier, K. Günter, H. Moritz, and T. Esslinger, Nature (London) **455**, 204 (2008).
[22] N. Strohmaier, D. Greif, R. Jördens, L. Tarruell, H. Moritz, T. Esslinger, R. Sensarma, D. Pekker, E. Altman, and E. Demler, Phys. Rev. Lett. **104**, 080401 (2010).
[23] U. Brandt and C. Mielsch, Z. Phys. B **75**,365 (1989).
[24] P. Werner, T. Oka, and A. J. Millis, Phys. Rev. B **79**, 035320 (2009).
[25] M. Schiró, Phys. Rev. B **81**, 085126 (2010).
[26] A. N. Rubtsov, V. V. Savkin, and A. I. Lichtenstein, Phys. Rev. B **72**, 035122 (2005).
[27] E. Gull, P. Werner, O. Parcollet, and M. Troyer, EPL **82**, 57003 (2008).
[28] P. Werner A. Comanac, L. de' Medici, M. Troyer, and A. J. Millis, Phys. Rev. Lett. **97**, 076405 (2006).
[29] Ph. Werner, T. Oka, M. Eckstein, and A. J. Millis, Phys. Rev. B **81**, 035108 (2010).
[30] H. Keiter and J. C. Kimball, Int. J. Magn. **1**, 233 (1971); J. Appl. Phys. **42**, 1460 (1971).
[31] N. Grewe and H. Keiter, Phys. Rev. B **24**, 4420 (1981).
[32] Y. Kuramoto, Z. Phys. B **53**, 37 (1983).

[33] S. E. Barnes, J. Phys. F. **6**, 1375 (1976).
[34] P. Coleman, Phys. Rev. B **29**, 3035 (1984).
[35] N. E. Bickers, D. L. Cox, and J. W. Wilkins, Phys. Rev. B **36**, 2036 (1987).
[36] N. E. Bickers, Rev. Mod. Phys. **59**, 845 (1987).
[37] E. Müller-Hartmann, Z. Phys. B **57**, 281 (1984).
[38] Th. Pruschke and N. Grewe, Z. Phys. B **74**, 439 (1989).
[39] K. Haule, S. Kirchner, J. Kroha, and P. Wölfle, Phys. Rev. B **64**, 155111 (2001).
[40] E. Gull, D. R. Reichman, and A. J. Millis, Phys. Rev. B **82**, 075109 (2010).
[41] Th. Pruschke, D. L. Cox, and M. Jarrell, Phys. Rev. B **47**, 3553 (1993).
[42] J. H. Shim, K. Haule, and G. Kotliar, Nature (London) **446**, 513 (2007).
[43] J. H. Shim, K. Haule, and G. Kotliar, Science **318**, 1615 (2007).
[44] K. Haule, C. Yee, and K. Kim, Phys. Rev. B **81**, 195107 (2010).
[45] P. Nordlander, M. Pustilnik, Y. Meir, N. S. Wingreen, and D. C. Langreth, Phys. Rev. Lett. **83**, 808 (1999).
[46] L. V. Keldysh, J. Exp. Theor. Phys. **47**, 1515 (1964); Sov. Phys. JETP **20**, 1018 (1965).
[47] For an introduction into the Keldysh formalism, see R. van Leeuwen, N. Dahlen, G. Stefanucci, C. Almbladh, and U. von Barth, arXiv:cond-mat/0506130 (unpublished); *Time-Dependent Density Functional Theory*, Lecture Notes in Physics Vol. 706, edited by M. A. L. Marques, C. A. Ullrich, F. Nogueira, A. Rubio, K. Burke, and E. K. U. Gross (Springer, Berlin 2006).
[48] H. Brunner and P. J. van der Houwen, *The Numerical Solution of Volterra Equations* (North-Holland, Amsterdam, 1986).
[49] J. W. Negele and H. Orland, *Quantum Many-Particle Systems* (Addison-Wesley, Redwood City, 1988).
[50] G. Baym and L. P. Kadanoff, Phys. Rev. **124**, 287 (1961); G. Baym, *ibid.* **127**, 1391 (1962).
[51] J. M. Luttinger and J. C. Ward, Phys. Rev. **118**, 1417 (1960).
[52] For a derivation of this equation in the nonequilibrium case, see M. Eckstein, A. Hackl, S. Kehrein, M. Kollar, M. Moeckel, P. Werner, and F. A. Wolf, Eur. Phys. J. Spec. Top. **180**, 217 (2010).
[53] N. Blümer, Ph.D. thesis, University of Augsburg, 2003.
[54] S. D. Huber and A. Rüegg, Phys. Rev. Lett. **102**, 065301 (2009).
[55] F. Hassler and S. D. Huber, Phys. Rev. A **79**, 021607(R) (2009).
[56] T. Oka, R. Arita, and H. Aoki, Phys. Rev. Lett. **91**, 066406 (2003); T. Oka, N. Konno, R. Arita, and H. Aoki, *ibid.* **94**, 100602 (2005).
[57] A. Albuquerque, F. Alet, P. Corboz, P. Dayal, A. Feiguin, S. Fuchs, L. Gamper, E. Gull, S. Gurtler, A. Honecker, R. Igarashi, M. Korner, A. Kozhevnikov, A. Lauchli, S. Manmana, M. Matsumoto, I. McCulloch, F. Michel, R. Noack, G. Pawlowski, L. Pollet, Th. Pruschke, U. Schollwock, S. Todo, S. Trebst, M. Troyer, P. Werner, and S. Wessel, J. Magn. Magn. Mater. **310**, 1187 (2007).